

Inverse scattering for frequency-scanned full-field optical coherence tomography

Daniel L. Marks, Tyler S. Ralston, Stephen A. Boppart, and P. Scott Carney

Beckman Institute of Advanced Science and Technology, 405 North Mathews, Urbana, Illinois 61801 USA

Received February 27, 2006; revised October 4, 2006; accepted October 25, 2006;
posted October 27, 2006 (Doc. ID 68379)

Full-field optical coherence tomography (OCT) is able to image an entire *en face* plane of scatterers simultaneously, but typically the focus is scanned through the volume to acquire three-dimensional structure. By solving the inverse scattering problem for full-field OCT, we show it is possible to computationally reconstruct a three-dimensional volume while the focus is fixed at one plane inside the sample. While a low-numerical-aperture (NA) OCT system can tolerate defocus because the depth of field is large, for high NA it is critical to correct for defocus. By deriving a solution to the inverse scattering problem for full-field OCT, we propose and simulate an algorithm that recovers object structure both inside and outside the depth of field, so that even for high NA the focus can be fixed at a particular plane within the sample without compromising resolution away from the focal plane. © 2007 Optical Society of America

OCIS codes: 100.3010, 110.4500.

1. INTRODUCTION

The capabilities of optical coherence tomography^{1,2} (OCT) and optical coherence microscopy^{3–5} (OCM) have been greatly extended by computed imaging and synthetic aperture techniques.⁶ Among the recently demonstrated advantages is the ability to resolve features in the sample that are outside the confocal region. Ultimately, a more quantitatively accurate and faithful representation of the sample structure is provided. In this work, the inverse scattering problem in full-field OCT–OCM^{7–15} is investigated. A variant where the focus remains fixed at the surface of the sample and computed imaging techniques are used to infer the structure is proposed. This modality obviates the requirement that the focus be scanned through the sample. A forward model is derived that relates the measured data to the object structure. From this model, a solution of the inverse scattering problem is obtained, thus providing a means to infer the object structure from the data. The achievable resolution and system bandpass are also derived. Finally, a simulation is presented that demonstrates the application of the method.

Full-field OCT is capable of imaging an entire plane of scatterers simultaneously, providing a very rapid way to acquire the sample structure. A typical full-field OCT system is built around a Michelson interferometer with a broadband illumination source (see Fig. 1). Reference and sample beams are derived from the source using a beam splitter. An extended area of the sample is illuminated by a broadband collimated beam through a microscope objective. The objective is focused at the depth of features of interest. A signal is scattered by the sample back through the objective. A reference beam is delayed to return to the beam splitter at the same time that the signal scattered from the sample in the focal plane arrives. The reference and signal are superimposed and focused on a focal-plane array (such as a CCD sensor) where the amplitude of the interference signal is measured. Only those scatterers

within a coherence length of the focal plane produce scattered fields that will interfere with the reference. By recording the interference, an image of a slice of the sample around the focal plane is obtained, and the out-of-focus contributions are removed by coherence gating. By translating the sample through the focal plane, the scatterers at many different depths may be imaged and a 3-D structure obtained.

While this method can be used to obtain high-resolution images for the entire volumes of a sample quickly, it has a number of disadvantages. First, the sample and microscope objective must be translated relative to each other. This is relatively slow and requires fine positioning. Second, this method uses time-domain detection that produces a lower signal-to-noise ratio than Fourier-domain or frequency-swept OCT.^{16–20}

When the reference arm is adjusted such that the reference field is synchronized with the scattered field returned from a plane other than (and far removed from) the focal plane, the interference image obtained at the CCD appears to be an image of the scatterers in that plane but out of focus. For a conventionally formed image, this would likely irreversibly impair the resulting image quality. However, wide-field OCT is an interferometric technique, and so the phase as well as the amplitude is measured. To bring an image into focus, it is simply necessary to appropriately rephase the field. To accomplish this, we will solve the linear inverse scattering problem. This serves the additional purpose of providing a quantitatively meaningful reconstruction of the entire object.

Instead of scanning the focus through the sample, we propose to fix the focus at the surface of the sample so that no relative translation is needed between the objective and the sample. A frequency-swept source can provide a new degree of freedom, replacing a degree of freedom lost by fixing the focus. Because the objective and sample may be left fixed relative to each other, no trans-

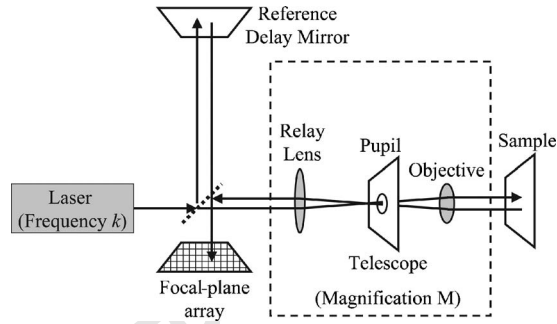


Fig. 1. Schematic diagram of full-field OCT using frequency scanning and the focus of the objective fixed at the sample surface.

91 lation hardware is needed, which makes placing the ob-
92 jective on a fiber optic or a handheld probe easier. While
93 frequency-swept full-field OCT²¹ has been achieved, typi-
94 cally the numerical aperture (NA) is low so that the depth
95 of field is very large and diffraction effects can be ne-
96 glected. However, when a high NA is used, the depth of
97 field is very short, and accounting for the defocus is nec-
98 essary to preserve the resolution over the entire volume of
99 interest.

100 To understand how computational image formation
101 works in full-field OCT, in Section 2 a physical model for
102 the scattering process is developed, and from this a rela-
103 tionship between the data and the object structure is de-
104 rived. Based on this relationship, in Section 3, the inverse
105 scattering problem is solved in order to infer the sample
106 structure from the data. In Section 4, an analysis of the
107 bandpass and resolving power of the system is given. In
108 Section 5, the results are illustrated by a numerical simu-
109 lation.

110 2. DERIVATION OF THE SCATTERING 111 OPERATOR FOR FULL-FIELD OPTICAL 112 COHERENCE TOMOGRAPHY

113 An illustration of the full-field OCT system being studied
114 is shown in Fig. 1. This system is based on a Michelson
115 interferometer, but other configurations such as a self-
116 referencing Fizeau design could be used. In this system,
117 the source is a tunable, narrowband laser. The laser is
118 tuned to wavelengths λ that correspond to wavenumbers
119 $k=2\pi/\lambda$. The laser ideally emits a plane wave (or is spa-
120 tially filtered to produce one).

121 The laser illumination is split into two. One component
122 travels to a reference mirror and is reflected back through
123 the beam splitter to the output port where the focal-plane
124 array is located. The other component is demagnified by a
125 factor $1/M$, using a telescope of magnification M . The pur-
126 pose of the telescope is to concentrate the illumination
127 onto the sample and then relay a magnified scattered field
128 to the focal-plane array. This telescope consists of two con-
129 verging lenses, a relay lens and a microscope objective.
130 The illumination on the sample is a normally incident
131 plane wave. The sample scatters some radiation back-
132 ward through the telescope. The telescope is aligned to
133 afocally and telecentrically image²² the front surface of
134 the sample to the focal-plane array. The telescope is in ef-
135 fect two Fourier-transform lenses with possibly nonunity

magnification.²³ Note that, unlike standard full-field OCT
microscopy, the focus of the objective remains fixed at the
surface of the sample. It is assumed that the telescope is
aberration free and vignetting inside the telescope is neg-
ligible. If the telescope is assumed to correct spherical ab-
erration, then there is a finite volume within the sample
space for which these assumptions hold. A pupil is placed
at the focus of the illumination beam inside the telescope
to spatially filter the backscattered signal to enforce a
well-defined spatial band limit. At the focal-plane array,
the reference and sample signals superimpose and inter-
fere, and the intensity of the interference is detected.

To derive the relationship between the object structure
and the data detected on the sensor, a mathematical
model of scattering of the illumination field by the object
and interferometric detection at the sensor is developed
below. A scalar field is substituted for the electromagnetic
field, neglecting polarization effects. The incident field on
the sample is given by the expression

$$E_i(\mathbf{r};k) = A(k)\exp(ik\mathbf{r} \cdot \hat{\mathbf{z}}), \quad (1)$$

where \mathbf{r} is a location in the sample volume, k is the illu-
mination wavenumber, $A(k)$ is the power spectral density
of the illumination at frequency k , and $\hat{\mathbf{z}}$ is the direction of
increasing depth into the sample. In this work, it is as-
sumed that the scattering is well modeled by the first
Born approximation. The susceptibility of the object is
given by $\eta(\mathbf{r})$ such that $\eta(\mathbf{r})=0$ for $z<0$. The secondary
scattered field $E_s(\mathbf{r}';k)$ from the object at the plane $z=0$ is
given by the expression

$$E_s(\mathbf{r}';k) = \int_V d^3r E_i(\mathbf{r};k) \eta(\mathbf{r}) \frac{\exp(ik|\mathbf{r}' - \mathbf{r}|)}{|\mathbf{r}' - \mathbf{r}|}. \quad (2)$$

It is useful to define the 2-D Fourier transform $\tilde{E}_s(\mathbf{q};k)$
 $= \int d^2r' E_s(\mathbf{r}';k) \exp(i\mathbf{q} \cdot \mathbf{r}')$ with \mathbf{q} being a transverse spa-
tial frequency such that $\mathbf{q} \cdot \hat{\mathbf{z}}=0$. Using the plane-wave ex-
pansion of a spherical wave, Eq. (2) is recast to read

$$\tilde{E}_s(\mathbf{q};k) = 2\pi i A(k) \int_V d^3r \eta(\mathbf{r}) \exp\{i[\mathbf{q} \cdot \mathbf{r}] + iz[k + k_z(\mathbf{q})]\} k_z(\mathbf{q})^{-1}, \quad (3)$$

where $k_z(\mathbf{q}) = \sqrt{k^2 - q^2}$. The 3-D Fourier transform is de-
fined such that $\tilde{\eta}(\mathbf{Q}) = \int_V d^3r \eta(\mathbf{r}) \exp(i\mathbf{Q} \cdot \mathbf{r})$. It is then
found that the right-hand integral can be expressed in
terms of $\tilde{\eta}(\mathbf{Q})$:

$$\tilde{E}_s(\mathbf{q};k) = 2\pi i A(k) k_z(\mathbf{q})^{-1} \tilde{\eta}(\mathbf{q} + \hat{\mathbf{z}}[k + k_z(\mathbf{q})]). \quad (4)$$

The field $E_f(\mathbf{r};k)$ is produced by the propagation of
 $E_s(\mathbf{r}';k)$ through the telescope to the focal-plane array.
Because the telescope is assumed to be an aberration-free
telescope that afocally and telecentrically images the
plane at the sample $z=0$ to the focal-plane array in the
plane $z=z_f$, its function can be modeled as a simple con-
volution with a point-spread function accounting for the
finite bandwidth of the telescope and a magnification fac-
tor given by M . The field at the focal-plane array is given
by $E_f(\mathbf{r};k)$, and the point-spread function of the telescope
is given by $P(\mathbf{r};k)$. The relationship between $E_f(\mathbf{r};k)$ and
 $E_s(\mathbf{r}';k)$ is thus

$$E_f(\mathbf{r};k) = M^{-1} \int d^2r' E_s(\mathbf{r}';k) P(\mathbf{r}/M - \mathbf{r}';k). \quad (5)$$

We further define the Fourier transforms $\tilde{E}_f(\mathbf{q};k) = \int_{z=z_f} d^2r E_f(\mathbf{r};k) \exp(i\mathbf{q} \cdot \mathbf{r})$ and the coherent transfer function of the telescope $\tilde{P}(\mathbf{q};k) = \int d^2r P(\mathbf{r};k) \exp(i\mathbf{q} \cdot \mathbf{r})$. Thus the convolution in Eq. (5) is expressed as

$$\begin{aligned} \tilde{E}_f(\mathbf{q};k) &= M \tilde{E}_s(M\mathbf{q};k) \tilde{P}(M\mathbf{q};k) \\ &= 2\pi i M A(k) \tilde{P}(M\mathbf{q};k) k_z(M\mathbf{q})^{-1} \tilde{\eta}(M\mathbf{q} + \hat{\mathbf{z}}[k \\ &\quad + k_z(M\mathbf{q})]). \end{aligned} \quad (6)$$

Equation (6) specifies a relationship between Fourier components of the field on the focal-plane array and those of the object susceptibility.

The reference mirror is placed to effect a delay of τ relative to the total delay required for the beam to travel from the beam splitter to the plane $z=0$ in the sample arm and back. The reference field $E_r(\mathbf{r};k, \tau)$ relayed to the focal-plane array is then given by

$$E_r(\mathbf{r};k, \tau) = A(k) \exp[i\omega(k)\tau], \quad (7)$$

where $\omega(k)$ is a dispersion relation relating the temporal frequency to the spatial frequency in the sample medium. For example, if the sample medium is vacuum, then $\omega(k) = kc$, where c is the speed of light in vacuum. The intensity $I(\mathbf{r};\mathbf{k}, \tau) = |E_r(\mathbf{r};k, \tau) + E_f(\mathbf{r};k)|^2$ on the focal-plane array is then given by the expression

$$\begin{aligned} I(\mathbf{r};k, \tau) &= |A(k)|^2 + |E_f(\mathbf{r};k)|^2 + 2A(k) \text{Re}\{E_f(\mathbf{r};k) \exp[\\ &\quad - i\omega(k)\tau]\}. \end{aligned} \quad (8)$$

The part of the signal that is due to interference between the signal and the reference beams is defined as the data function $D(\mathbf{r};k) = A(k)E_f(\mathbf{r};k)$. The complex quantity $D(\mathbf{r};k)$ can be estimated from measurements of $I(\mathbf{r};k, \tau)$ at multiple values of the delay τ . For example, three measurements of $I(\mathbf{r};k, \tau)$ such that $\omega\tau = 0, \pi/2$, and π may be summed to yield

$$D(\mathbf{r};k) = \frac{1-i}{4} I(\mathbf{r};k, 0) - \frac{1+i}{4} I(\mathbf{r};k, \pi/\omega) + \frac{i}{2} I(\mathbf{r};k, \pi/2\omega). \quad (9)$$

This method of phase-shifting interferometry is well known.²⁴ Inserting the results of Eq. (6), we can express the Fourier transform of the data function, which is $\tilde{D}(\mathbf{q};k) = \int d^2r D(\mathbf{r};k) \exp(i\mathbf{q} \cdot \mathbf{r})$, as

$$\tilde{D}(\mathbf{q};k) = \tilde{K}(\mathbf{q};k) \tilde{\eta}(M\mathbf{q} + \hat{\mathbf{z}}[k + k_z(M\mathbf{q})]), \quad (10)$$

where for convenience the bandpass function \tilde{K} is defined

$$\tilde{K}(\mathbf{q}, k) = 2\pi i M A(k)^2 \tilde{P}(M\mathbf{q};k) k_z^{-1}(M\mathbf{q}). \quad (11)$$

Thus the data are expressed in terms of the 3-D Fourier transform of the sample structure, and so the resolution of the reconstruction of the sample structure is space invariant. However, vignetting and aberrations in the telescope limit the volume over which this resolution can be obtained. As long as the center of the volume of interest is

along the axis of the objective and on the focal plane of the objective, and the extent of the volume is much smaller than the field size the objective is corrected for, the aberrations and vignetting of the telescope can be neglected, and the resolution can be considered space invariant. However, for a sufficiently large volume of interest the resolution of the instrument becomes space variant and sensitive to the specific vignetting and aberration properties of the objective used.

When obtaining an inverse scattering solution, it is desirable to express Eq. (10) in the operator notation used for formal statements of relationships between functions because formal inverse scattering solutions are commonly expressed in terms of such operators. We define an operator $\tilde{\mathbf{K}}$ such that $\tilde{\mathbf{D}} = \tilde{\mathbf{K}}\tilde{\eta}$, which relates the sample susceptibility Fourier representation $\tilde{\eta}$ to the data Fourier representation $\tilde{\mathbf{D}}$ with the relationship of Eq. (10). We define the axial component of $\beta = \mathbf{Q} \cdot \hat{\mathbf{z}}$ and the transverse component of \mathbf{Q} as $\mathbf{Q}_{\parallel} = \mathbf{Q} - \hat{\mathbf{z}}\beta$. The operator $\tilde{\mathbf{K}}$ is then given by

$$\begin{aligned} \tilde{\mathbf{D}} &= \tilde{\mathbf{K}}\tilde{\eta} \\ &= \int d^3\mathbf{Q} \tilde{K}(\mathbf{q};k) \tilde{\eta}(\mathbf{Q}) \delta^{(2)}(\mathbf{Q}_{\parallel} - M\mathbf{q}) \delta[\beta - k - k_z(M\mathbf{q})], \end{aligned} \quad (12)$$

where the delta functions enforce the conditions of the coordinate transformation. This operator concisely contains both the kernel and the coordinate transformations expressed in Eq. (10).

To obtain the measurements needed to reconstruct $\eta(\mathbf{r})$, one must vary both k and τ . In practice, however, it is often slow and inconvenient to adjust both. If one is willing to tolerate some image artifacts, just one of these parameters need be scanned. For simplicity, it is assumed that the pupil function $P(\mathbf{r}';k)$ is real and symmetric, which is often the case (for example, with a circular pupil), so that $\tilde{P}(\mathbf{q};k)$ is likewise real and symmetric.

One may decide to hold the reference delay position fixed such that $\tau=0$ to avoid translating the mirror. In this case phase shifting is not performed, and the imaginary component of $D(\mathbf{r};k)$ is not obtainable. If the imaginary part of $D(\mathbf{r};k)$ is assumed to be zero, then due to the Hermitian symmetry of the Fourier transform of real functions $\tilde{D}(-\mathbf{q}, k) = \tilde{D}(\mathbf{q}, k)^*$. The function $\tilde{\eta}(\mathbf{Q})$ then also has Hermitian symmetry reflected over the axis $|\mathbf{q}|=0$. The effect is that a conjugate image of the susceptibility is present, reflected across the plane $z=0$. Because the delay $\tau=0$ corresponds to the plane $z=0$, as long as the entire sample is contained in the half-space $z>0$, the conjugate image and the real image do not overlap. In addition, there is an artifact corresponding to the term $|E_f(\mathbf{r};k)|^2$ in Eq. (8). If the magnitude of the sample signal is small relative to the reference signal, the magnitude of this artifact is also small compared with the real image and can be neglected.

For completeness, we note that the method of inverse scattering can be applied to time-domain full-field OCT as well. If the delay τ is scanned as occurs in time-domain full-field OCT and the laser emits all wavenumbers k simultaneously (such as occurs in a mode-locked laser or a

291 spontaneous emission source typical of time-domain
292 OCT), the signal $I_T(\mathbf{r}; \tau)$ is the sum of the interference
293 patterns over all emitted frequencies:

$$I_T(\mathbf{r}; \tau) = \frac{1}{2\pi} \left[\int_{-\infty}^{\infty} dk \left(\frac{d\omega}{dk} \right) (|A(k)|^2 + |E_r(\mathbf{r}; k)|^2) \right] + \frac{1}{\pi} \operatorname{Re} \left\{ \int_{-\infty}^{\infty} dk \left(\frac{d\omega}{dk} \right) D(\mathbf{r}; k) \exp[-i\omega(k)\tau] \right\}. \quad (13)$$

296 The term in square brackets is a background intensity
297 that is independent of τ and therefore is easily subtracted
298 to remove its contribution from the measured intensity.
299 Neglecting the background intensity and the slowly vary-
300 ing Jacobian ($d\omega/dk$), Eq. (13) relates the real part of the
301 inverse Fourier transform of $D(\mathbf{r}; k)$ with respect to k to
302 the total intensity $I_T(\mathbf{r}; \tau)$. To be able to remove the $\operatorname{Re}\{\}$
303 operation so that a unique solution for $D(\mathbf{r}; k)$ can be
304 found, one equates $D(\mathbf{r}; -k) = D(\mathbf{r}; k)^*$. Equation (10) then
305 likewise enforces Hermitian symmetry on $\eta(-\mathbf{Q}) = \eta(\mathbf{Q})^*$.
306 Therefore in this case the reconstructed susceptibility is
307 assumed to be real valued.

308 In this derivation, the focal plane of the objective and
309 the front surface of the sample are assumed to coincide.
310 This assumption has simplified the preceding analysis
311 and presentation, but it is not required. If the sample is
312 placed such that the focus is below the sample surface by
313 a distance z_0 , but the delay produced by the reference co-
314 incides with the delay of the sample surface, the data can
315 be modified to account for the displacement. In particular,
316 the modified data $\tilde{D}'(\mathbf{q}; k)$ are related to the sampled data
317 $\tilde{D}(\mathbf{q}; k)$ by

$$\tilde{D}'(\mathbf{q}; k) = \tilde{D}(\mathbf{q}; k) \exp\{iz_0[k - k_z(M\mathbf{q})]\}. \quad (14)$$

319 This formula can be found by noting that the field relayed
320 by the telescope is now situated at the plane $z = z_0$, intro-
321 ducing a factor $\exp\{-iz_0[k + k_z(M\mathbf{q})]\}$ to the right-hand
322 side of Eq. (3). At the same time, the delay reference mir-
323 ror must be moved a distance z_0 further from the beam
324 splitter so that the new effective delay corresponds to the
325 front surface of the sample, including a factor of \exp
326 $\{-2ikz_0\}$ to the right-hand side of Eq. (7) to place the ref-
327 erence delay coincident with the front surface of the
328 sample. Effectively, the measured field is computationally
329 propagated at each frequency to the surface of the
330 sample.

331 3. INVERSE SCATTERING IN FULL-FIELD 332 OPTICAL COHERENCE TOMOGRAPHY

333 Using the developed mathematical model, a solution to
334 the inverse scattering problem may be derived. In gen-
335 eral, the problem is ill posed, and so regularization tech-
336 niques will need to be used to produce a stable solution.
337 Because the forward problem is linear, we derive a linear-
338 ized inverse based on least-squares error. To do so, we
339 first specify the complete forward operator \mathbf{K} such that
340 $\mathbf{D} = \mathbf{K}\eta$, which relates the data to the object structure

$$D(\mathbf{r}; k) = \mathbf{K}\eta = \int d^3r' K(\mathbf{r}', \mathbf{r}; k) \eta(\mathbf{r}'), \quad (15)$$

where the kernel $K(\mathbf{r}'; \mathbf{r}; k)$ of the operator \mathbf{K} is given by

$$K(\mathbf{r}', \mathbf{r}; k) = M^{-1} A(k)^2 \exp(ik\mathbf{r}' \cdot \hat{\mathbf{z}}) \times \int_{\mathbf{r}'' \cdot \hat{\mathbf{z}}=0} d^2r'' \frac{\exp(ik|\mathbf{r}'' - \mathbf{r}'|)}{|\mathbf{r}'' - \mathbf{r}'|} P(\mathbf{r}/M - \mathbf{r}''; k). \quad (16)$$

Given this relationship between the data and the object, the pseudoinverse solution $\eta^+(\mathbf{r})$ for object susceptibility is

$$\eta^+(\mathbf{r}) = \arg \min_{\eta} |\mathbf{D} - \mathbf{K}\eta|^2 = \arg \min_{\eta} \int d^2r' \int dk |D(\mathbf{r}'; k) - \mathbf{K}\eta(\mathbf{r}')|^2. \quad (17)$$

Expressed in operator notation, the solution to this least-squares problem is given by the pseudoinverse $\eta^+ = (\mathbf{K}^\dagger \mathbf{K})^{-1} \mathbf{K}^\dagger \mathbf{D}$, where \mathbf{K}^\dagger is the Hermitian conjugate of \mathbf{K} and $\mathbf{K}^\dagger \mathbf{K}$ is assumed to be invertible. It is much simpler to formulate the least-squares problem in the Fourier domain, using the operator $\tilde{\mathbf{K}}$ of Eq. (12). In terms of the operator $\tilde{\mathbf{K}}$, the Tikhonov-regularized least-squares solution $\tilde{\eta}^+ = (\tilde{\mathbf{K}}^* \tilde{\mathbf{K}} + \gamma \mathbf{I})^{-1} \tilde{\mathbf{K}}^* \tilde{\mathbf{D}}$, with $\tilde{\mathbf{K}}^*$ being the adjoint operator to $\tilde{\mathbf{K}}$ and the positive constant γ being the regularization parameter. The adjoint is explicitly given by the expres-
360

$$\tilde{\eta}_A = \tilde{\mathbf{K}}^* \tilde{\mathbf{D}} = \int d^2q \int dk \tilde{\mathbf{K}}^*(\mathbf{q}; k) \tilde{D}(\mathbf{q}; k) \delta^{(2)}(\mathbf{Q}_\parallel - M\mathbf{q}) \delta[k - k_z(M\mathbf{q})] = \tilde{\mathbf{K}}^* \left(M^{-1} \mathbf{Q}_\parallel; \frac{Q_\parallel^2 + \beta^2}{2\beta} \right) \tilde{D} \times \left(M^{-1} \mathbf{Q}_\parallel; \frac{Q_\parallel^2 + \beta^2}{2\beta} \right) M^{-2} \frac{\beta}{\beta + \sqrt{\beta^2 + Q_\parallel^2}}, \quad (18)$$

with $\tilde{\mathbf{K}}(\mathbf{q}; k)$ taken from Eq. (11). Given the expressions for $\tilde{\mathbf{K}}$ and $\tilde{\mathbf{K}}^*$, the solution $\tilde{\eta}^+$ is given by

$$\tilde{\eta}^+(\mathbf{Q}) = \frac{\tilde{D} \left(M^{-1} \mathbf{Q}_\parallel; \frac{Q_\parallel^2 + \beta^2}{2\beta} \right) \tilde{\mathbf{K}}^* \left(M^{-1} \mathbf{Q}_\parallel; \frac{Q_\parallel^2 + \beta^2}{2\beta} \right)}{\left| \tilde{\mathbf{K}} \left(M^{-1} \mathbf{Q}_\parallel; \frac{Q_\parallel^2 + \beta^2}{2\beta} \right) \right|^2 + \gamma M^2 \frac{\beta + \sqrt{\beta^2 + Q_\parallel^2}}{\beta}}. \quad (19)$$

4. RESOLUTION AND BANDPASS

Equation (10) expresses a relationship between the 2-D Fourier transform of the data and the 3-D Fourier transform of the object. As mentioned previously, this relationship implies that the resolution of the reconstructed ob-
372

373 ject is space invariant. With suitable specifications of the
374 instrument, one can identify the region of the Fourier
375 space of the structure function that can be sampled. This
376 region is called the band volume and is an analogue to the
377 band limit of 1-D signals, except that the band volume
378 consists of the interior of a shape in 3-D Fourier space
379 rather than just a 1-D interval.

380 There are two specifications of the instrument that de-
381 termine the shape of the band volume. The first is the
382 bandwidth of the illumination, which is specified by the
383 interval of frequencies $k_{min} < k < k_{max}$. The other param-
384 eter is the numerical aperture (NA) of the imaging system
385 $0 < NA < 1$. A particular NA implies a pupil bandpass:

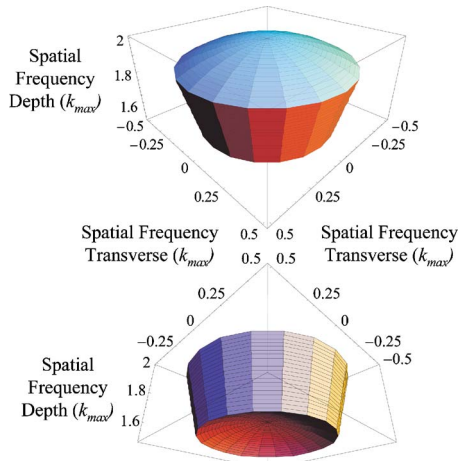
$$386 \quad \tilde{P}(\mathbf{q};k) = 1 \quad \text{for } |\mathbf{q}| \leq (NA)k, \\ 387 \quad \tilde{P}(\mathbf{q};k) = 0 \quad \text{for } |\mathbf{q}| > (NA)k. \quad (20)$$

388 These inequalities constrain the volume of the data func-
389 tion $\tilde{D}(\mathbf{q};k)$ that can be sampled. The band volume is the
390 intersection of the volumes defined by the two inequali-
391 ties expressed in terms of the object 3-D spatial frequency
392 \mathbf{Q} :

$$393 \quad k_{min} < \mathbf{Q}^2 / (2\mathbf{Q} \cdot \hat{\mathbf{z}}) < k_{max}, \\ 394 \quad (2\mathbf{Q} \cdot \hat{\mathbf{z}}) \sqrt{\mathbf{Q}^2 - (\mathbf{Q} \cdot \hat{\mathbf{z}})^2} / \mathbf{Q}^2 < NA. \quad (21)$$

395 Figure 2 shows an example of a band volume for an in-
396 strument with 0.5 NA and bandwidth from $0.8k_{max} < k$
397 $< k_{max}$. There are two views so that both the top and the
398 bottom surfaces are visible. The top and bottom surfaces
399 are spherical (with different radii and centers), and the
400 side surface is a right circular cone with its vertex at the
401 origin.

402 In the limit of small bandwidth and low NA, the band
403 volume shape approaches that of a circular cylinder. In
404 this limit, the resolution in the axial direction is deter-
405 mined solely by the bandwidth, and the transverse reso-
406 lution is determined by the NA, as is normally assumed in
407 OCT. However, the band volume becomes less cylindrical
408 and more cone shaped as the NA and bandwidth increase,



Color: Online Fig. 2. (Color online) Calculated band volume shape for a full-field OCT system. All units are in terms of the maximum spatial frequency of the illumination.

and axial and transverse resolutions are dependent on both the bandwidth and the NA.

5. SIMULATION

To demonstrate the expected performance of inverse scattering in full-field OCT, a simulation was performed. An object consisting of randomly placed point scatterers was imaged with a simulated full-field OCT system, and then the structure of the object was reconstructed from the data. The simulated object volume cross-sectional area was 25 wavelengths in depth and 40 by 40 wavelengths in the transverse direction. The illumination source had a Gaussian spectrum with a 40% fractional full width at half-maximum bandwidth (corresponding, for example, to 320 nm of bandwidth centered at 800 nm, which can be achieved by a Ti-sapphire laser).^{25–27} The simulated NA of the imaging objective was 0.5.

Data were synthesized by first calculating the scattered field $E_s(\mathbf{r}';k)$ using Eq. (2), where the object $\eta(\mathbf{r})$ was taken to be a collection of randomly chosen discrete points. The synthetic interferograms were calculated as a function of illumination spatial frequency that corresponds to how the data would be acquired from a swept source. Then the synthesized data function was calculated using the relation $\tilde{D}(\mathbf{q};k) = A(k)\tilde{E}_s(\mathbf{q};k)\tilde{P}(\mathbf{q};k)$, where $\tilde{E}_s(\mathbf{q};k)$ was obtained from $E_s(\mathbf{r}';k)$ by a 2-D Fourier transform. Finally, a 2-D inverse Fourier transform yielded $D(\mathbf{r}';k)$. By assembling the synthetic data by superimposing the signals produced by discrete scatterers, the accuracy of the resampling-based inverse method could be better verified because the synthetic data were computed without resampling.

The synthetic data are shown in Fig. 3. Figure 3(a) shows $D(\mathbf{r};k)$, which describes the data that would be recorded on the focal-plane array. Because this is difficult to interpret, we have also included in Fig. 3(b) the time-domain signal $I_T(\mathbf{r};\tau)$ given by Eq. (13), which appears to more directly represent the underlying object. It may be seen in the plots of $I_T(\mathbf{r};\tau)$ that as the delay τ is increased the planes more distant from the focus are acquired and manifest increasing distortion. This corresponds to the standard degradation one expects from defocus when inverse scattering is not used.

The following steps were followed to compute the image estimate $\eta^+(\mathbf{r})$ from the synthetic data $D(\mathbf{r};k)$:

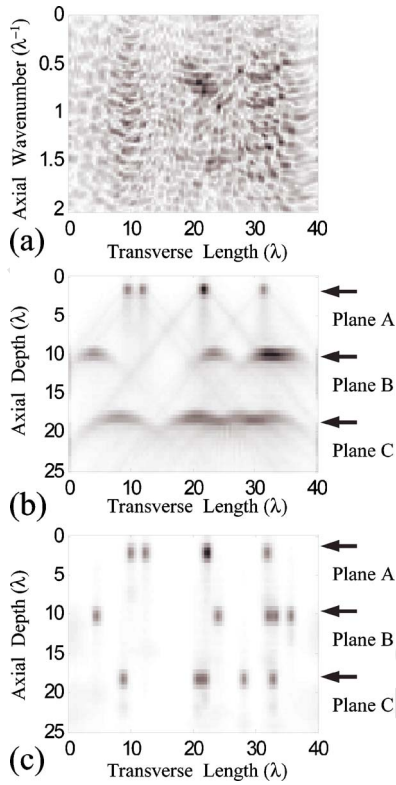
1. $\tilde{D}(\mathbf{q};k)$ was computed from $D(\mathbf{r};k)$ using the 2-D Fourier transform.

2. The kernel $\tilde{K}(\mathbf{q};k)$ was calculated using Eq. (11).

3. Equation (19) was used to compute $\tilde{\eta}^+(\mathbf{q};k)$ from $\tilde{K}(\mathbf{q};k)$ and $\tilde{D}(\mathbf{q};k)$.

4. The function $\tilde{\eta}^+(\mathbf{q};k)$, which is uniformly sampled in the variables \mathbf{q} and k , is resampled to be uniformly sampled in the variables \mathbf{q} and β using the relation $k = (M^2q^2 + \beta^2)/2\beta$. The resampled version is $\tilde{\eta}^+(\mathbf{Q})$, where the transverse component of \mathbf{Q} is $M\mathbf{q}$ and the axial component is β .

5. The 3-D inverse Fourier transform of $\tilde{\eta}^+(\mathbf{Q})$ is performed to find $\eta(\mathbf{r})$.



Color: Online
 Fig. 3. (Color online) Simulation of inverse scattering in full-field OCT. (a) The magnitude of the raw interference patterns recorded as a function of illumination spatial frequency. (b) A projection of the time-domain data for a collection of randomly placed point scatterers imaged with full-field OCT. (c) A projection of the computed reconstruction of the scatterers. All length units are in the center wavelength of the illumination, and spatial frequencies are inverse wavelength units. Three planes are denoted that are shown as *en face* images in Fig. 5.

466 The resampling step (step 4) is the key step in compen-
 467 sating for out-of-focus diffraction effects and therefore
 468 needs further discussion. Equation (10) specifies a rela-
 469 tionship between $\tilde{D}(\mathbf{q};k)$ and $\tilde{\gamma}(\mathbf{Q})$. In the continuously
 470 sampled case, there is a one-to-one correspondence be-
 471 tween values of \tilde{D} and $\tilde{\gamma}$ so that this relation is straight-
 472 forward. However, in practice the data $D(\mathbf{r};k)$ is dis-
 473 cretely sampled and is typically uniform in \mathbf{r} and k . The
 474 Fourier data $\tilde{D}(\mathbf{q};k)$ are therefore sampled uniformly in \mathbf{q}
 475 and k . However, the reconstructed Fourier data of the
 476 susceptibility $\tilde{\gamma}^+(\mathbf{Q})$ need to be uniform in \mathbf{q} and β so that
 477 the 3-D inverse Fourier transform can recover a uni-
 478 formly sampled reconstruction of $\eta(\mathbf{r})$. The resampling
 479 step interpolates points on the function $\tilde{\gamma}^+(\mathbf{q};k)$ that are
 480 uniformly spaced in β . Figure 4 is a plot of the points on a
 481 given function that are sampled in the forward and in-
 482 verse problems. Each of the intersections of grid curves
 483 indicates a point on the function that is interpolated to
 484 form the resampled function. Figure 4(a) is the resam-
 485 pling that maps from 3-D object space $\mathbf{Q}_{\parallel},\beta$ to the data
 486 space \mathbf{q},k for the forward problem. Figure 4(b) is the re-
 487 sampling from the data space \mathbf{q},k to the object space
 488 $\mathbf{Q}_{\parallel},\beta$. The resampling occurs only along lines of constant
 489 \mathbf{q} , so that only 1-D interpolation is needed. In this simu-
 490 lation, a 1-D cubic B-spline interpolator was used to in-
 491 terpolate from the coordinates $\mathbf{q}+\hat{z}[k+k_2(\mathbf{q})]$ to \mathbf{Q} as
 492 shown in Eq. (19).

493 Finally, after the 3-D inverse Fourier transform of
 494 $\tilde{\gamma}^+(\mathbf{Q})$ is taken, the reconstruction $\eta^+(\mathbf{r})$ results, which is
 495 shown in Fig. 3(c). As can be seen, the reconstruction cor-
 496 rects for diffraction and produces pointlike images. Figure
 497 5 shows three *en face* planes corresponding to the depths
 498 A, B, and C marked in Fig. 3. The left column is the time-
 499 domain data measured in each of the *en face* planes, and
 500 the right column is the image of the scatterers computed
 501 by inverse scattering. Planes that are further from the fo-
 502 cus appear to exhibit poorer resolution when viewed in
 503 the raw data because of the effect of defocus. One can also
 504 see the interference fringes between the images of adja-
 505 cent scatterers. Despite the interference between scatter-
 506 ers, each point is clearly resolved with space-invariant
 507 resolution in the reconstructed image. This shows the al-
 508 gorithm correctly separates the interference patterns

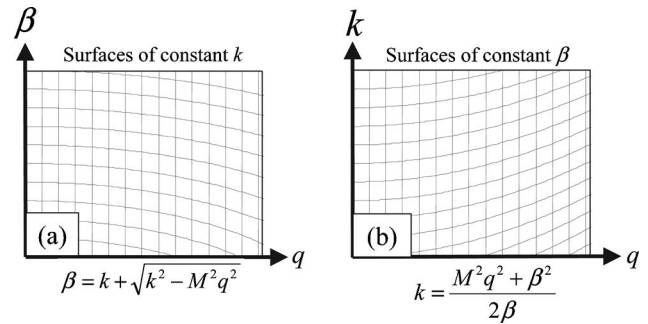
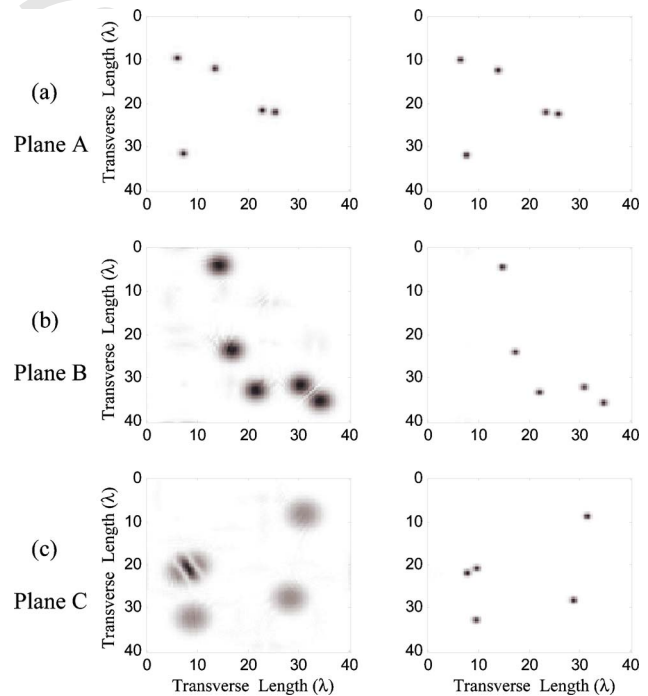
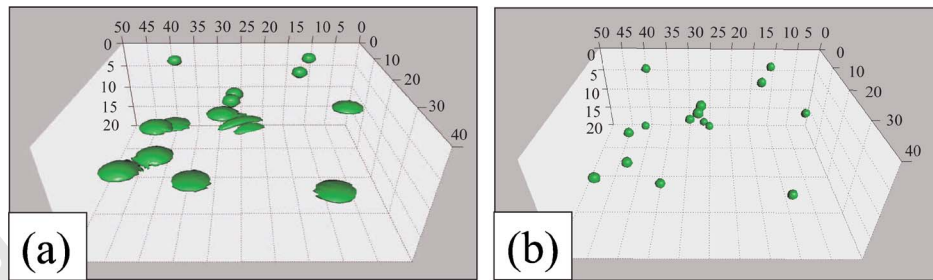


Fig. 4. (a) Resampling grid to compute synthetic data $\tilde{D}(\mathbf{q};k)$ from object $\tilde{\gamma}(\mathbf{Q})$. (b) Resampling grid to compute reconstruction of $\tilde{\gamma}(\mathbf{Q})$ from $\tilde{D}(\mathbf{q};k)$. Note that the transverse components of \mathbf{Q} are the same as $M\mathbf{q}$, and the axial component of \mathbf{Q} is β . To form the full 3-D Fourier space, both grids are revolved around their respective vertical axes.



Color: Online
 Fig. 5. (Color online) Three pairs of *en face* images of the time-domain data (left) and the reconstructed volume (right). (a)–(c) Pairs of images corresponding, respectively, to the planes A, B, and C marked in Fig. 3. All dimensions are in wavelength units.



Color: Online Fig. 6. (Color online) Three-dimensional volumes representing the (a) time-domain data and (b) reconstructed volume. All dimensions are in wavelength units.

509 from scatterers to produce high-resolution images.
 510 To show the overall improvement to the data, Fig. 6 is
 511 volume isosurface plots of the raw data in Fig. 6(a) and
 512 the reconstructed computed image in Fig. 6(b). Again, the
 513 blurring of the data is increasingly apparent with increas-
 514 ing distance from the focus plane at the top of the volume.
 515 In addition, stripelike features can be seen for the isosur-
 516 faces corresponding to interfering scatterers. This method
 517 can correct for the diffraction effects and produce point-
 518 like images in Fig. 6(b) for each of the scatterers. The
 519 planes of the scatterers need not be so widely separated
 520 for the algorithm to distinguish them, but this was delib-
 521 erately done to make the diffraction effects easier to visu-
 522 alize.

523 6. CONCLUSION

524 We have derived and demonstrated a method of perform-
 525 ing inverse scattering in full-field OCT to reconstruct im-
 526 ages of out-of-focus planes, which obviates the need to
 527 scan the focus through the volume. The solution of the in-
 528 verse scattering problem implies that, neglecting vignett-
 529 ing and aberrations, the achievable resolution is space in-
 530 variant and is the same away from the focus plane as at
 531 the focal plane. Vignetting limits the volume over which
 532 the resolution is space invariant because the solid angle
 533 over which the scattered light is collected decreases at
 534 points further from the objective aperture. Other factors
 535 limiting reconstruction quality are multiple scattering
 536 within the sample and sample motions during data acqui-
 537 sition causing phase error. This method may lead to faster
 538 and more accurate full-field OCT imaging because data
 539 acquisition can be very rapid, requiring only that the 2-D
 540 interferogram be sampled while the frequency of the
 541 source is scanned. As data acquisition speed and compu-
 542 tational speed continue to increase, perhaps video-rate
 543 scanning of 3-D volumes will become possible.

544 Inverse scattering in full-field OCT also offers a signal-
 545 to-noise advantage over scanned beam OCT. In conven-
 546 tional scanned beam OCT, which utilizes a focused Gauss-
 547 ian beam rather than plane-wave illumination, it was
 548 shown⁶ that the magnitude of the signal captured from
 549 scatterers away from the focus is inversely proportional to
 550 the distance from the focus. In practice, this places a limit
 551 on the axial range of the sample that can be imaged be-
 552 fore the signal-to-noise ratio becomes unacceptable. There
 553 is no such attenuation of the signal away from the focus
 554 in the full-field OCT case. However, this advantage may
 555 be offset because full-field OCT may be less able to dis-

criminate between single-scattering and multiply scatter- 556
 ed photons because of its multimode detection. 557

ACKNOWLEDGMENTS 558

This research was supported in part by the American 559
 Heart Association (0355396Z, S. A. Boppart) and the Na- 560
 tional Institutes of Health (National Institute of Biomed- 561
 ical Imaging and Bioengineering) (1 R01 EB00108, S. A. 562
 Boppart). P. S. Carney is supported in part by a National 563
 Science Foundation Faculty Early Career Development 564
 (CAREER) award. Additional information can be found at 565
<http://biophotonics.uiuc.edu/>. 566

S. A. Boppart can be reached by phone, 1-217-244-7479; 567
 fax, 1-217-244-1995; or e-mail, boppart@uiuc.edu. D. L. 568
 Marks can be reached by e-mail at dmarks@uiuc.edu. 569

REFERENCES 570

1. D. Huang, E. A. Swanson, C. P. Lin, J. S. Schuman, W. G. 571
 Stinson, W. Chang, M. R. Hee, T. Flotte, K. Gregory, C. A. 572
 Puliafito, and J. G. Fujimoto, "Optical coherence 573
 tomography," *Science* **254**, 1178–1181 (1991). 574
2. S. A. Boppart, B. E. Bouma, C. Pitris, J. F. Southern, M. E. 575
 Brezinski, and J. G. Fujimoto, "In vivo cellular optical 576
 coherence tomography imaging," *Nat. Med.* **4**, 861–864 577
 (1998). 578
3. J. A. Izatt, M. R. Hee, G. M. Owen, E. A. Swanson, and J. 579
 G. Fujimoto, "Optical coherence microscopy in scattering 580
 media," *Opt. Lett.* **19**, 590–592 (1994). 581
4. J. M. Schmitt, M. J. Yadlowsky, and R. F. Bonner, 582
 "Subsurface imaging of living skin with optical coherence 583
 microscopy," *Dermatology (Basel, Switz.)* **191**, 93–98 584
 (1995). 585
5. J. A. Izatt, H.-W. Kulkarni, K. Wang, M. W. Kobayashi, and 586
 M. W. Sivak, "Optical coherence tomography and 587
 microscopy in gastrointestinal tissues," *IEEE J. Sel. Top.* 588
Quantum Electron. **2**, 1017–1028 (1996). 589
6. T. S. Ralston, D. L. Marks, P. S. Carney, and S. A. Boppart, 590
 "Inverse scattering problem for optical coherence 591
 tomography," *J. Opt. Soc. Am. A* **23**, 1027–1037 (2006). 592
7. E. Beaurepaire and A.-C. Boccara, "Full-field optical 593
 coherence microscopy," *Opt. Lett.* **23**, 244–246 (1998). 594
8. A. Dubois, L. Vabre, A.-C. Boccara, and E. Beaurepaire, 595
 "High-resolution full-field optical coherence tomography 596
 with a Linnik microscope," *Appl. Opt.* **41**, 805–812 (2002). 597
9. A. Dubois, K. Grieve, G. Moneron, R. Lecaque, L. Vabre, 598
 and C. Boccara, "Ultrahigh-resolution full-field optical 599
 coherence tomography," *Appl. Opt.* **43**, 2874–2883 (2004). 600
10. A. Dubois, G. Moneron, K. Grieve, and A.-C. Boccara, 601
 "Three-dimensional cellular-level imaging using full-field 602
 optical coherence tomography," *Phys. Med. Biol.* **49**, 603
 1227–1234 (2004). 604
11. K. Grieve, A. Dubois, M. Simonutti, M. Paques, J. Sahel, 605
 J.-F. Le Gargasson, and C. Bocarra, "In vivo anterior 606
 segment imaging in the rat eye with high speed white light 607

- 608 full-field optical coherence tomography,” *Opt. Express* **13**,
609 6286–6295 (2005).
- 610 12. B. Laude, A. De Martino, B. Drevillon, L. Benattar, and L.
611 Schwartz, “Full-field optical coherence tomography with
612 thermal light,” *Appl. Opt.* **41**, 6637–6645 (2002).
- 613 13. G. Moneron, A.-C. Bocarra, and A. Dubois, “Stroboscopic
614 ultrahigh-resolution full-field optical coherence
615 tomography,” *Opt. Lett.* **30**, 1351–1353 (2005).
- 616 14. J. Moreau, V. Lorlette, and A.-C. Bocarra, “Full-field
617 birefringence imaging by thermal-light polarization-
618 sensitive optical coherence tomography. II. Instrument and
619 results,” *Appl. Opt.* **42**, 3811–3818 (2003).
- 620 15. Y. Watanabe, Y. Hayasaka, M. Sato, and N. Tanno, “Full-
621 field optical coherence tomography by achromatic phase
622 shifting with a rotating polarizer,” *Appl. Opt.* **44**,
623 1387–1392 (2005).
- 624 16. R. Leitgeb, C. K. Hitzenberger, and A. F. Fercher,
625 “Performance of Fourier domain vs. time domain optical
626 coherence tomography,” *Opt. Express* **11**, 889–894 (2003).
- 627 17. M. Choma, M. Sarunic, Y. Changhuei, and J. Izatt,
628 “Sensitivity advantage of swept source and Fourier domain
629 optical coherence tomography,” *Opt. Express* **11**,
630 2183–2189 (2003).
- 631 18. P. Blazkiewicz, M. Gourlay, J. R. Tucker, A. D. Rakic, and
632 A. V. Zvyagin, “Signal-to-noise ratio study of full-field
633 Fourier-domain optical coherence tomography,” *Appl. Opt.*
634 **34**, 7722–7729 (2005).
- 635 19. A. V. Zvyagin, “Fourier-domain optical coherence
tomography: optimization of signal-to-noise ratio in full
space,” *Opt. Commun.* **242**, 97–108 (2004).
20. A. V. Zvyagin, P. Blazkiewicz, and J. Vintrou, “Image
reconstruction in full-field Fourier-domain optical
coherence tomography,” *J. Opt. A* **7**, 350–356 (2005).
21. B. Povazay, A. Unterhuber, B. Hermann, H. Sattmann, H.
Arthaber, and W. Drexler, “Full-field time-encoded
frequency-domain optical coherence tomography,” *Opt.
Express* **14**, 7661–7669 (2006).
22. D. N. Sitter, Jr. and W. T. Rhodes, “Three-dimensional
imaging: a space invariant model for space variant
systems,” *Appl. Opt.* **29**, 3789–3794 (1990).
23. J. Goodman, *Introduction to Fourier Optics* (McGraw-Hill,
1968).
24. P. Hariharan, *Optical Interferometry* (Academic, 2003).
25. B. E. Bouma, G. J. Tearney, S. A. Boppart, M. R. Hee, M. E.
Brezinski, and J. G. Fujimoto, “High-resolution optical
coherence tomographic imaging using a mode-locked
Ti:Al₂O₃ laser,” *Opt. Lett.* **20**, 1486–1488 (1995).
26. W. Drexler, U. Morgner, F. X. Kartner, C. Pitris, S. A.
Boppart, X. Li, E. P. Ippen, and J. G. Fujimoto, “*In vivo*
ultrahigh-resolution optical coherence tomography,” *Opt.
Lett.* **24**, 1221–1223 (1999).
27. D. L. Marks, A. L. Oldenburg, J. J. Reynolds, and S. A.
Boppart, “Study of an ultrahigh-numerical-aperture fiber
continuum generation source for optical coherence
tomography,” *Opt. Lett.* **27**, 2010–2012 (2002).

AUTHOR QUERIES — 514704JOA

#1 Au: Please confirm that NIBIB and CAREER were written out correctly.

PROOF COPY [68379] 514704JOA